Original article

Investigation of RC-DTH air hammer performance using CFD approach with dynamic mesh method

Xinxin Zhang [a], Yongjiang Luo [b,c,*], Liming Fan [d], Jianming Peng [e], Kun Yin [e]

[a] Key Laboratory of Ministry of Education on Metallogenic Prediction of Nonferrous Metals and Geological Environment Monitoring, Central South University, Changsha 410083, China
[b] State Key Laboratory of Coal Mine Disaster Dynamics and Control, College of Resources and Environmental Science, Chongqing University, Chongqing 400044, China
[c] Hunan Provincial Key Laboratory of Shale Gas Resource Utilization, Hunan University of Science and Technology, Xiangtan 411201, China
[d] CCDC Drilling & Production Engineering Technology Research Institute, PetroChina, Deyang 618000, China
[e] Key Laboratory of Drilling and Exploitation Technology in Complex Conditions, Ministry of Land and Resources, Jilin University, Changchun 130026, China

HIGHLIGHTS

- RC-DTH air hammer drilling technology to enhance drilling efficiency.
- CFD approach with dynamic-mesh method was presented.
- Dynamic layering, sliding interfaces, and user defined functions were used to update the mesh.
- Impacting performance of the RC-DTH air hammers was studied numerically.
- Piston mass should be optimal to match with the designed geometric parameters.

GRAPHICAL ABSTRACT
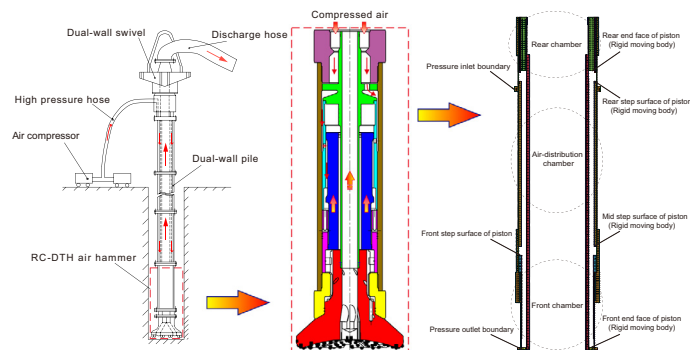
Performance analysis of RC-DTH air hammer using CFD approach with dynamic mesh method.

ARTICLE INFO

ABSTRACT

Reverse circulation down-the-hole (RC-DTH) air hammers have been widely used in construction and mining activities owing to their high drilling efficiency and good dust control performance. This paper presents a computational fluid dynamics (CFD) approach with the dynamic mesh method for evaluating the performance of RC-DTH air hammers. Nine stages of operating conditions of the RC-DTH air hammer are described herein to better understand the operating mechanism of the RC-DTH air hammer. Dynamic layering, sliding interfaces, as well as user-defined functions were employed to update the mesh in dynamic mesh modelling. The influences of rebound coefficient, input air pressure, and piston mass on the performance of RC-DTH air hammers were studied. It was found that increasing the rebound coefficient and input air pressure can improve the impact performance of RC-DTH air hammers, whereas increasing input air pressure can reduce energy efficiency and increase energy consumption. In addition, simulation results indicate that increasing the input air pressure may increase the stroke of the piston; the piston mass should be optimally selected to match the designed geometric parameters to avoid a significant drop in performance. The CFD approach with the dynamic mesh method shows superiority in evaluating the performance of RC-DTH air hammers.

Introduction

Percussion drilling is considered as one of the best approaches to hard rock drilling owing to its several advantages over conventional rotary drilling [1–3]. Certain representative advantages among these are the improved rate of penetration (ROP) and reduction in the non-productive time associated with high bit consumption, excessive trips, and stuck pipe [4,5]. Moreover, the total contact time of the drill bit inserted into a rock is shorter than that in rotary drilling, resulting in a higher instantaneous weight-on-bit (WOB), even though the mean WOB may be maintained at lower levels for drilling [6]. Straighter holes and low costs per metre are achieved by the percussion action effect [7]. Therefore, this type of drilling has been widely used in mining and has also expanded to oil and gas drilling operations since more and more oil and gas reservoirs are under hard rock formations [8].

The reverse circulation down-the-hole (RC-DTH) air hammer is an innovative percussion drilling tool driven by air [9]. During drilling, compressed air is injected into the annulus of the dual-wall pipes and drives the RC-DTH hammer to implement high-frequency blows acting on a reverse circulation drill bit where the reverse circulation is formed. A striking feature of this drilling method is the combination of percussion drilling with the reverse circulation drilling technique. As shown in Fig. 1, drill cuttings are carried by the compressed air in a reverse circulation manner, i.e. cuttings travel directly from the bottom of the borehole to the surface through the central passage of the drill pipes. Using reverse circulation can eliminate many disadvantages associated with normal air drilling. A main difference is the capability to drill in broken or fractured formations [10]. Low air consumption and the consequent capability in large-diameter-hole drilling is another benefit. Since formation cores are returned continuously to the surface without having to stop drilling, a higher core recovery rate is achieved. Particularly, as the air and rock cuttings exhausted from the flexible discharging hose can be guided directly into the cuttings and dust collector unit placed far from the drill site, the operating environment is improved and the atmosphere is oil-free, thus hindering the drill workers and equipment from the threat of drilling dust [11,12].

Most previous efforts on RC-DTH air hammer drilling focused on the performance of reverse circulation drill bits aimed at obtaining a better design to enhance the capability of reverse circulation (or dust control performance). Yin et al. [11] investigated a reverse circulation drill bit with suction nozzles set on the ribs of the bit. In their work, the effect of geometric parameters in terms of number, inclination, and location of suction nozzles on the dust control performance were analysed. Luo et al. [12] performed a series of experimental studies with an orthogonal design to obtain the optimal parameters for a specially designed reverse circulation drill bit; a dust control efficiency of up to 99% was recorded in their study. Furthermore, Cao et al. [13] proposed a design with a swirling generator on the drill bits; Wu et al. [14] introduced supersonic nozzles to the reverse circulation drill bit. These studies concluded that the capability of reverse circulation for the drill bits with proper design was at a satisfactory level. Nevertheless, studies on the performance of the RC-DTH air hammer remain primarily unexplored.

The penetration rate of the RC-DTH air hammer drilling depends heavily on the impacting performance of the RC-DTH hammer. For this drilling method to be adopted in even wider applications, the impacting performance, in terms of impact energy per blow, impact frequency, and power output must be improved continuously. The design of the RC-DTH air hammer based on the conventional experimental method and empirical design is time consuming and costly; thus, satisfactory results are difficult to obtain. Computational fluid dynamics (CFD) has been used widely in nuclear industry [15], chemical engineering [16,17] and oil and gas drilling operations [18–20] and is one of the most promising approaches to return accurate predictions on RC-DTH air hammer performance. It is able to model multi-dimensional geometries and resolves the effects introduced by individually integrated components. The structural details of the RC-DTH air hammer can be considered in a CFD simulation.

The objective of this study is to investigate the effects posed by some of the important geometrical and operational parameters on the performance of a RC-DTH air hammer using a three-dimensional CFD model. Considering that the air flows in the hammer tool interact with the mechanical component, thus resulting in a complex coupling relationship between them, a dynamic mesh method was proposed and used in this study to make the coupled flow-structure analysis possible.

Description of the RC-DTH air hammer

As shown in Fig. 2, the RC-DTH air hammer mainly consists of a central tube, an inner casing, a piston, a spacer bush, an outer tube, etc. The movement of the piston can be described as two phases:
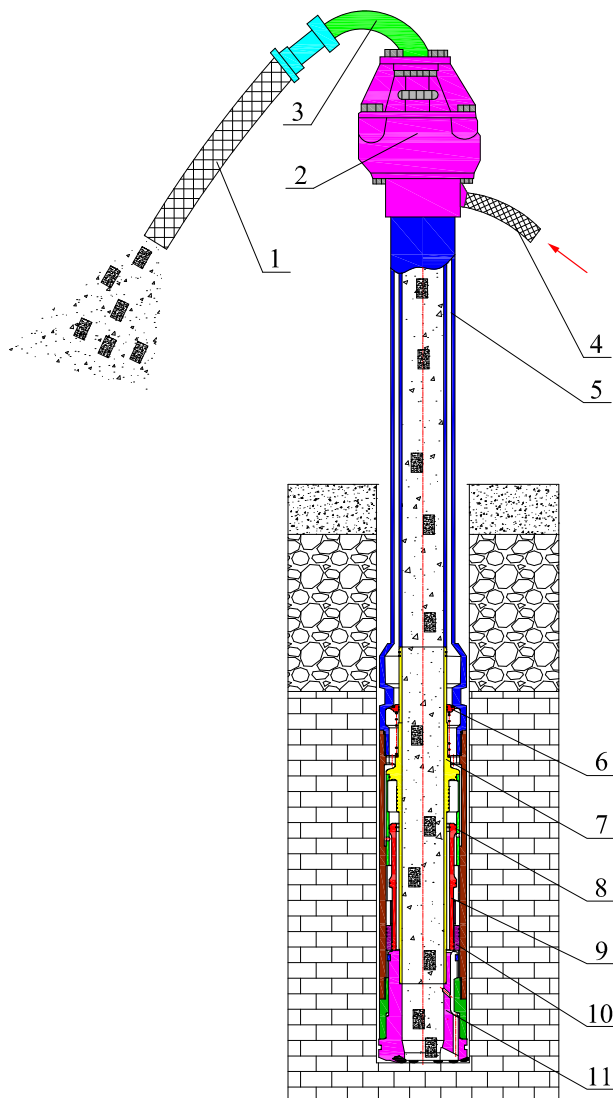

Fig. 1. Schematic of RC-DTH air hammer drilling system. 1: flexible discharging hose; 2: dual-wall swivel; 3: goose neck tube; 4: flexible air input tube; 5: dual-wall drill pipe; 6: check valve; 7: centre tube; 8: inner casing; 9: piston; 10: spacer bush; and 11: reverse circulation drill bit.
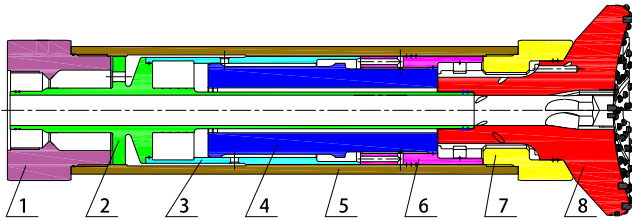
Fig. 2. Main parts in RC-DTH air hammer. 1: upper connection; 2: centre tube; 3: inner casing; 4: piston; 5: outer tube; 6: spacer bush; 7: splined hub; and 8: drill bit.

the backhaul phase and the stroke phase, and each phase experiences air intake, air expansion, air compression, and air exhaust stages.

As depicted in Fig. 3 and Table 1, at the initial stage *a*, compressed air flows into the front chamber and pushes the piston to move backward; air in the rear chamber is exhausted to the bottom hole. When the piston displacement is larger than L_{ro} (stage *b*), air in the rear chamber starts to be compressed as the exhaust

Fig. 3. Schematic of RC-DTH air hammer (some structures are simplified to render them concise and intelligible): (a), (b), (c), (d), and (e) represent the backhaul phase and (f), (g), (h), and (i) represent the stroke phase; the end of (e) can be regarded as the initial stage of the stroke phase and the end of (i) as the initial stage of the backhaul phase; Table 1 lists the air conditions in each stage.

Table 1
Positioning logic and air conditions at each stage.

Stages	Piston displacement L	Air conditions (front air chamber)	Air conditions (rear air chamber)
a	$0 \leq L < L_{ro}$	Air intake ($\dot{m}_f>0$)	Air exhaust ($\dot{m}_r<0$)
b	$L_{ro} \leq L < L_{fi}$	Air intake ($\dot{m}_f>0$)	Air compression ($\dot{m}_r=0$)
c	$L_{fi} \leq L \leq L_{roc}$	Air expansion ($\dot{m}_f=0$)	Air compression ($\dot{m}_r=0$)
d	$L_{roc} < L \leq L_{fie}$	Air expansion ($\dot{m}_f=0$)	Air intake ($\dot{m}_r>0$)
e	$L_{fie} < L \leq L_{max}$	Air exhaust ($\dot{m}_f<0$)	Air intake ($\dot{m}_r>0$)
f	$L_{roc} < L \leq L_{fie}$	Air compression ($\dot{m}_f=0$)	Air intake ($\dot{m}_r>0$)
g	$L_{fi} \leq L \leq L_{roc}$	Air compression ($\dot{m}_f=0$)	Air expansion ($\dot{m}_r=0$)
h	$L_{ro} \leq L < L_{fi}$	Air intake ($\dot{m}_f>0$)	Air expansion ($\dot{m}_r=0$)
i	$0 \leq L < L_{ro}$	Air intake ($\dot{m}_f>0$)	Air exhaust ($\dot{m}_r<0$)

Note: L_{ro}, L_{fi}, L_{roc}, L_{fie}, and L_{max} represent certain key locations in the piston where the air conditions change at each stage; in particular, L_{max} represents the actual stroke of piston; $\dot{m}_f$ represents the instantaneous air mass flow rate passing through the front chamber; and $\dot{m}_r$ represents the instantaneous air mass flow rate passing through the rear chamber (shown in Fig. 3).

passage is blocked by the rear end face of the piston. At stage *c* ($L_{fi} \leq L \leq L_{roc}$), when the mid-step surface of the piston passes through the front step surface of the inner casing, air stops flowing into the front chamber and air in the front chamber begins to expand, thus pushing the piston to move backward, continuously. As the piston displacement is larger than L_{roc} at stage *d*, the rear step surface of the piston passes through the rear step surface of the inner casing, and compressed air flows into the rear chamber to implement an opposite force acting on the piston such that the backward moving piston stops to move forward. Stage *e* is the condition where the air in the front chamber is exhausted and the piston stops at L_{max}, thus reaching its maximal rear end position, and is about to move forward. This is typically some distance away from the centre tube body to avoid impact; hence, the actual stroke is not constant and may vary with the varying geometrical and operational parameters of the RC-DTH air hammer. After the directional change at stage *e*, the piston is accelerated towards the drill bit. Air conditions at stages *f*, *g*, *h*, and *i* are similar to those of stages *d*, *c*, *b*, and *a*, respectively, except for the compression and expansion conditions opposing the conditions in the backhaul phase. After the impact occurs at the end of stage *i*, stage *a* will become active again and a new work cycle begins.

Numerical methodology and procedure

Chen et al. studied the velocity field of a fluidic DTH hammer using CFD dynamic analysis [21]. Peng et al. [22] reported a CFD study to investigate the effect of geometric parameters on the performance of a fluidic DTH hammer. Zhang et al. [23,24] demonstrated an improvement by considering the external flow field of the piston-hammer within the CFD calculation models to enhance the accuracy of the simulation results for a high-energy version of the fluidic hammer. It was proven that CFD simulations using the dynamic mesh method can identify some geometrical parameters affecting the performance of the fluidic DTH hammers, and provide a promising approach to clarify the motion process of the piston in the f RC-DTH air hammer.

In this work, the dynamic mesh method was adopted in the CFD simulations and a user-defined function was added into the CFD code, 'ANSYS Fluent', allowing for cell positions, velocities, and accelerations at each time step to be obtained and used in functions to calculate various pressure-induced loads in the model.

Selection of turbulence model

Flows in the RC-DTH air hammer are relatively simple. Turbulent effects in the current model are considered using the Spalart–Allmaras turbulence model. Bao et al. [25] found that using this model can yield good results for predicting the aerodynamic characteristics of prismatic cylinders. Although the Spalart–Allmaras turbulence model is not always recommended for numerical simulations of compressible flows, other models, e.g. the standard κ–ε turbulence or RNG-based κ–ε turbulence model, may better describe the internal flow in a RC-DTH air hammer but do not necessarily outperform the Spalart–Allmaras turbulence model in terms of overall performance prediction. Because the main objective is performance maximisation through numerical calculations, and the moderate and similar levels of accuracy (result differences among them are less than 4%) in predicting the RC-DTH air hammer performance can be obtained irrespective of the turbulence models selected, the Spalart–Allmaras turbulence model was chosen for its robustness, ease in convergence (the convergence time of Spalart-Allmaras turbulence model is about 1/3 of the others), and reasonable accuracy in modelling turbulent flow in RC-DTH air hammers.
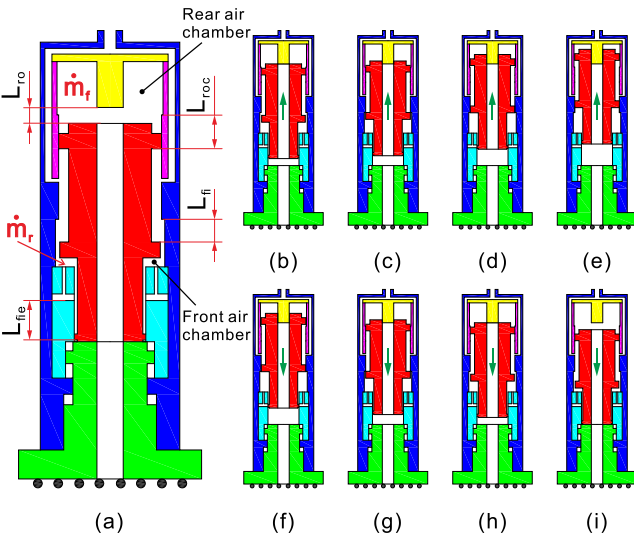
Governing equations for flow

Compressible flows can be described by employing the mass and momentum conservation equations.

Mass conservation:

$$\frac{\partial \rho}{\partial t} + \nabla \cdot (\rho \overrightarrow{v}) = 0 \tag{1}$$

Momentum conservation:

$$\frac{\partial}{\partial t}(\rho \overrightarrow{v}) + \nabla \cdot (\rho \overrightarrow{v} \overrightarrow{v}) = -\nabla p + \nabla \cdot (\bar{\bar{\tau}}) + \rho \overrightarrow{g} + \overrightarrow{F} \tag{2}$$

where ρ is the density; $\overrightarrow{v}$ is the mean velocity, p is the static pressure, $\rho \overrightarrow{g}$ is the gravitational body force, and $\overrightarrow{F}$ is the external body forces. Stress tensor $\bar{\bar{\tau}}$ is given by:

$$\bar{\bar{\tau}} = \mu \left[(\nabla \overrightarrow{v} + \nabla \overrightarrow{v}^{\mathrm{T}}) - \frac{2}{3} \nabla \cdot \overrightarrow{v} I \right] \tag{3}$$

where μ denotes molecular viscosity, I denotes the unit tensor, and the second term on the right hand side is the effect of volume dilation.

Furthermore, considering the conservation of energy, a general form of the governing equations, can be expressed as:

$$\frac{\partial(\rho \phi)}{\partial t} + div(\rho \mu \phi) = div(\Gamma grad \phi) + S \tag{4}$$

where ϕ denotes the dependent variable, u denotes the velocity vector, Γ denotes the diffusion coefficient, and S is the general source term.

The transported variable in the Spalart–Allmaras model, $\tilde{v}$, is identical to the turbulent kinematic viscosity except in the near-wall region. The transport equation for $\tilde{v}$ is

$$\frac{\partial \tilde{v}}{\partial t} + \frac{\partial}{\partial x_{\mathrm{i}}}(\rho \tilde{v} u_{\mathrm{i}}) = G_v + \frac{1}{\sigma \tilde{v}} \left[\frac{\partial}{\partial x_{\mathrm{j}}} \left\{ (\mu + \rho \tilde{v}) \frac{\partial \tilde{v}}{\partial x_{\mathrm{j}}} \right\} + C_{b2} \rho \left(\frac{\partial \tilde{v}}{\partial x_{\mathrm{j}}} \right)^2 \right]$$
$$- Y_v + S_{\tilde{v}} \tag{5}$$

where G_v is the production of turbulent viscosity; Y_v is the destruction of turbulent viscosity occurring in the near-wall region; $\sigma \tilde{v}$ and C_{b2} are constants; v is the molecular kinematic viscosity; $S_{\tilde{v}}$ is a user-defined source term.

Mathematical model for deforming mesh

By the driven compressed air, the piston moves back and forth rapidly. The boundary positions of the flow domains change with the piston movement by using the technique of the dynamic mesh model. The general form of the conservation equation for a general scalar ϕ, and a control volume V with a movable boundary can be written as follows:

$$\frac{d}{dt} \int_v \rho \phi dV + \int_{\partial V} \rho \phi (\overrightarrow{u} - \overrightarrow{u}_g) \cdot d\overrightarrow{A} = \int_{\partial V} \Gamma \nabla \phi \cdot d\overrightarrow{A} + \int_V S_{\phi} dV \tag{6}$$

where ρ is the density of fluid; $\overrightarrow{u}$ is the flow velocity vector; $\overrightarrow{u}_g$ is the moving mesh grid velocity; Γ is the diffusion coefficient; S_{ϕ} is the source term of ϕ; ∂V represents the boundary of the control volume V.

The first term in Eq. (6) can use a first-order backward difference formula to yield the following:

$$\frac{d}{dt} \int_V \rho \phi dV = \frac{(\rho \phi V)^{\mathrm{n}+1} - (\rho \phi V)^{\mathrm{n}}}{\Delta t} \tag{7}$$

where n and $n + 1$ represent the respective quantity at the current and next time step values, respectively. Further, $V^{\mathrm{n}+1}$ denotes the $(n + 1)$th time step volume and can be computed from

$$V^{\mathrm{n}+1} = V^{\mathrm{n}} + \frac{dV}{dt} \Delta t \tag{8}$$

Governing equation for piston movement

Forces acting on the piston mainly consist of gravity and pressure-induced forces. Other forces such as body forces, flow-induced forces, and friction forces are sufficiently low such that they can be ignored in this calculation. The force balance equation of the piston is given by Newton's second law as follows:

$$m \frac{d^2 X}{dt^2} = P_{rs} A_{rs} - P_{ms} A_{ms} + P_{fs} A_{fs} + P_{fe} A_{fe} - P_{re} A_{re} - mg \tag{9}$$

where A_{rs} denotes the displacement area of the rear step surface of the piston; A_{ms} denotes the displacement area of the mid step surface of piston; A_{fs} denotes the displacement area of the front step surface of piston; A_{fe} denotes the displacement area of the front end face of piston; P_{re} denotes the displacement area of the rear end face of the piston. P_{rs}, P_{ms}, P_{fs}, P_{fe}, and P_{re} are the corresponding pressure differences acting on the areas. Additionally, m is the piston mass, g is the acceleration of gravity, i.e. g = 9.18 m/s^2.

When impact occurs at the stroke end, the rebound velocity v of the piston is calculated by

$$v = -k \overrightarrow{v}_{\mathrm{i}} \tag{10}$$

where k is the rebound coefficient; $\overrightarrow{v}_{\mathrm{i}}$ is the piston impact velocity.

When the time step is sufficiently small, the piston acceleration can be considered to be constant in each time step. Thus, the piston velocity v^{n+1} for the $(n + 1)$th time step can be calculated by

$$v^{n+1} = v^n + a^n \Delta t \tag{11}$$

where a^n denotes the $(n + 1)$th time step acceleration of the piston.

Furthermore, the piston displacement $X^{\mathrm{n}+1}$ for the $(n + 1)$th time step can be obtained from

$$X^{\mathrm{n}+1} = X^{\mathrm{n}} + \left(\frac{v^{\mathrm{n}} + v^{\mathrm{n}+1}}{2} \right) \Delta t = X^{\mathrm{n}} + v^{\mathrm{n}} \Delta t + \frac{a^n \Delta t^2}{2} \tag{12}$$

Computational domain and grid independence

The computational domain of flow in a typical RC-DTH air hammer mainly includes the flow field of the rear and front air chambers, air-distribution chamber, air inlet, and outlet passages. All these computational domains are interconnected directly or by the leakage gaps between the cylindrical mating surfaces to satisfy the iteration requirement of the continuity equation. Fig. 4 shows a typical grid model of the RC-DTH air hammer. In this grid, all the cells are hexahedron; this is considered to be beneficial for achieving higher calculation efficiency and better accuracy.

Grid independence was conducted using the grid convergence index (GCI) method as described by Celik et al. [26]. In this analysis, three meshes with different densities were constructed: a coarse grid with 263,336 cells; medium grid with 405,140 cells; fine grid with 918,752 cells. The impact frequency was used to calculate the GCI index. Table 2 presents the main parameters calculated in the GCI approach. According to Table 2, the numerical uncertainty associated with the fine and medium grid solutions for the impact frequency was <0.4%. The apparent order was 15.93 with a GCI index of 5.15×10^{-3}% for fine grid and 0.393% for the medium grid. The extrapolated value for the impact frequency is 16.339, which is close to the corresponding value obtained for the fine grid. Thus, all simulations in this work were conducted based on the medium grid owing to its lower computational cost.
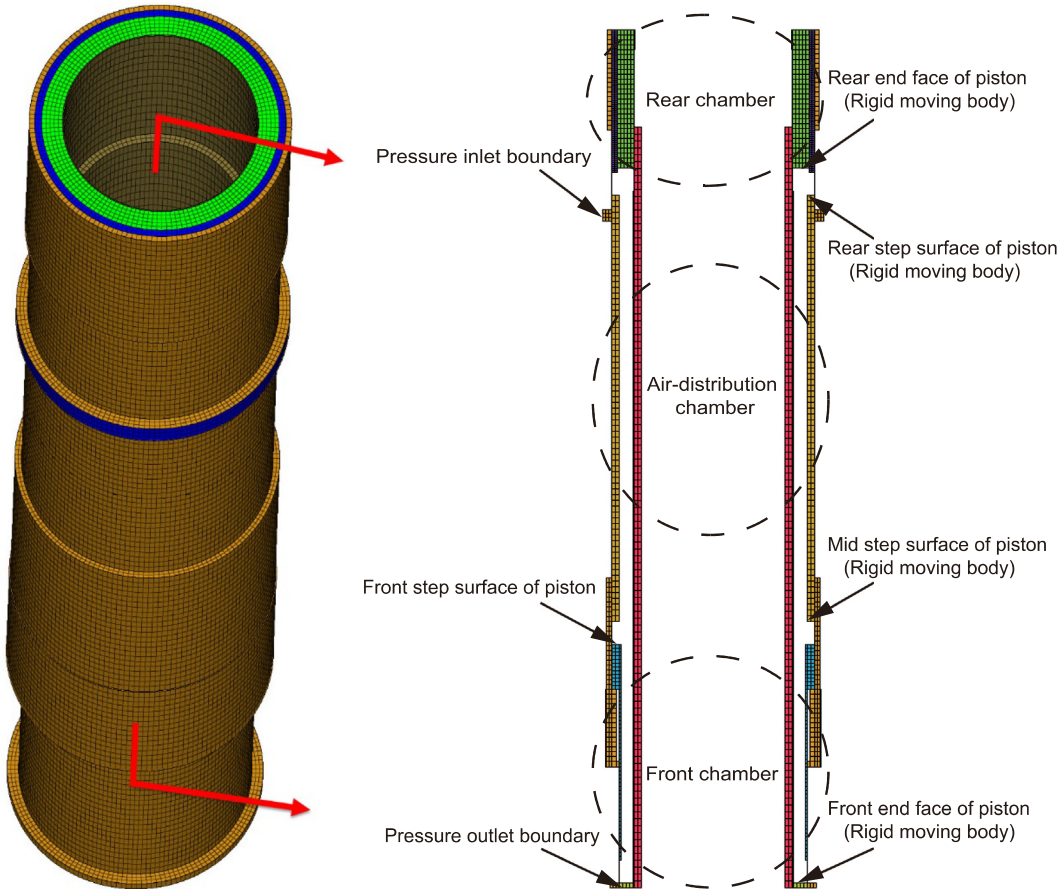
Fig. 4. Typical grid model of flow domain and boundary conditions.

Table 2
GCI estimation for impact frequency (Indices 1, 2, and 3 refer to fine, medium, and coarse grids, respectively).

Parameters	ϕ = Impact frequency (Hz)
$N_1/N_2/N_3$	918, 752/405, 140/263, 336
r_{21}/r_{32}	1.31/1.15
ϕ_1	16.34
ϕ_2	16.39
ϕ_3	16.81
p	15.93
ϕ^{ext}	16.339
e_{21}^a	0.003
e_{32}^a	0.026
e_{21}^{ext}	6.12×10^{-5}
e_{32}^{ext}	3.12×10^{-3}
GCI_{21}	5.15×10^{-3}%
GCI_{32}	0.393%

Boundary conditions and solver setting

Both steady and unsteady simulations were conducted in the simulation process, and the steady computational result is used as the initial condition for unsteady simulation. As shown in Fig. 4, pressure-inlet and pressure-outlet boundary conditions were used in the computational models of RC-DTH air hammers. The non-slip boundary condition was adopted at other boundaries. Because of the compressibility of air flows, the ideal-gas model predefined in ANSYS Fluent was used as the fluid material. The momentum and continuity equations were solved by a pressure-based coupled solver in a closely coupled manner. The time step

for the unsteady probability marker equation is calculated automatically based on the Courant Number that is specified as 1 and Explicit Relaxation Factors for momentum and pressure that are both specified as 0.1. Under-Relaxation Factors were used by the pressure-based solver to control the update of computed variables at each iteration, and all of the under-relaxation factors in this study are specified as 0.1 to ensure convergence of the simulation. A second-order upwind discretization was used for the calculation of both the turbulent kinetic energy and turbulent dissipation rate to obtain better results. The time step should be set at a suitable value to describe the movement of the piston and to ensure that the time cost of each simulation is acceptable. In this study, the time step of the 1E-4s is an acceptable value and yields satisfactory results for the current simulations.

Dynamic mesh and user-defined function

In the unsteady simulations, the piston motion changes the flow zones immediately next to them; therefore, the computational domain should be updated in each time step. The dynamic layering method provided by ANSYS Fluent was used to update the grid domain in the deforming regions influenced by the movement of the piston. As displayed in Fig. 4, the moving boundaries, i.e. the two end faces and three step surfaces of the piston were defined as moving rigid bodies. The corresponding projected zones influenced by the moving rigid bodies are defined as deforming zones. The update of the grid in the dynamic mesh method is handled automatically at each time step based on the new positions of the piston. As the five moving boundaries of the piston are internal zones, implying that the adjacent zones are maintained static while the piston is moving, elements projected to the moving rigid

bodies (deforming zones) should be separated and of different element layer heights with the adjacent zones. The coupled sliding interfaces in Fluent were used in these elements to transit from the deforming elements to the adjacent non-deforming elements.

Furthermore, user-defined functions (UDFs) based on the governing equation for piston movement, which are written by C programming, were employed to update the grid domain. The UDFs can obtain the position of the moving rigid body in real time, and the volume mesh will update according to the piston position. The DEFINE macro DEFINE_CG_MOTION was used to implement the dynamic mesh update. The average element facet pressures exerted on the rigid bodies were calculated at each time step. The pressure-induced forces, velocity, acceleration, and displacements of the piston can be obtained from the simulations.

Results and discussion

The GQ-142 reverse circulation DTH air hammer was used as a case study in this work; it has a nominal outer diameter of 142 mm. The effects of input air pressure on the impact frequency, impact energy, and energy efficiency of the RC-DTH air hammer were investigated. The effect of piston mass on the impact energy and impact frequency was also studied. Fig. 5 shows the typical pressure magnitude contours at different time steps for the simulation of a GQ-142 RC-DTH air hammer. The simulation results indicate a considerable agreement with the description in Table 1.

Effects of rebound coefficient on the impacting performance

The rebound coefficient k is considered as the ratio of rebound velocity to the impact velocity of the piston (shown in Eq. (10)). It is generally an empirical value related to the property of drilled formations. Li et al. reported that the rebound of the DTH hammer increases approximately linearly with the hardness of the rock [27]. Analyses by Zhang et al. [18] revealed that the piston impact frequency varied up to 30% depending on the rebound effect in a fluidic DTH hammers.

As shown in Fig. 6a and b, with an increase in the rebound coefficient, both the impact velocity and stroke of the piston increase. The impact velocity varies by approximately 18%, while the impact frequency exhibits an increase of approximately 6%. The increasing level of impact frequency appears to be low compared with previous studies; this underestimate may be attributed to the simulation results that only cover two operating periods of the piston. The rebound effect has not been accumulated to a steady level. The decreased impact performance with decreasing rebound coefficient confirms the fact that hammer tools typically demonstrate pool performance in drilling soft formations. The variation in piston stroke is approximately 13%. To prevent the piston from striking the centre tube, it should be imposed a sufficient distance away from the centre tube body according to the predicted value.

Effects of input air pressure on the performance of the RC-DTH air hammer

Fig. 6c shows the variations in the velocity of the piston in an approximate impact period. The input air pressure P varies from 1.6 MPa to 2.2 MPa with the gradient of 0.2 MPa. As shown, the impact velocity (the corresponding velocity at the impact points) of the piston increases with increasing input air pressure P. In particular, the piston velocity increases with time until the piston displacement $L > L_{roc}$. Subsequently, the piston decelerates and moves to the backward stroke end. A reverse increase in velocity begins with the forward movement of the piston until the piston displacement $L < L_{ro}$; subsequently, the piston decelerates and moves to the

forward stroke end where the impact occurs. The mean increase rate in velocity in the negative direction is higher than that in the positive direction. This is attributed to the fact that the direction of the forward movement (negative direction) is in accordance with the gravitational direction, and that the air-acting area of the piston in the rear chamber is larger than that in the front chamber.

Fig. 6d indicates the simulation results of the case $P = 2.2$ MPa. The operating conditions of the piston can be identified according to the characteristics of the curves. In stages a and b, the acceleration of the piston remains nearly constant. While the piston moves continuously and reaches stage c, the acceleration decreases slightly. This represents the end of the air intake condition taking place in the front chamber and the air expansion is now triggered. Subsequently, the acceleration decreases significantly and reaches a relative steady value in the negative direction. This represents the characteristics of stages d and e; stage e ends up with the piston reaching its maximum value of displacement (the piston stroke). As the backhaul phase is complete and the stroke phase begins, variations in the piston acceleration and displacement show the opposite trend. Referring to Fig. 6d, it can be also noted that the peak velocity occurs prior to the normal impact point of the tool. The deceleration of the piston prior to the impact represents a source of inefficiency; this inefficiency can be reduced by the optimal design but cannot be eradicated owing to the specific operating mechanism of the RC-DTH air hammer.

Simon [28] obtained an experimental relation between the ROP and power output P, of a drilling process:

$$S = 2.4 \frac{P_{im} - P_{im0}}{D^2 w} \tag{13}$$

where S is the penetration rate, D is the gauge (diameter), and w is the strength of the rock. P_{im0} is the threshold power and is almost negligible for sharp wedges or soft rocks but may be rather large for hard formations. $P_{im} = Ef$ (E denotes the impact energy per blow and can be obtained by $E = 0.5 \, mV_{im}^2$, where V_{im} denotes the piston impact velocity) for a DTH hammer drilling. As shown, $S \propto Ef$. Therefore, the impact energy per blow E and impact frequency f are critical for evaluating the performance of the RC-DTH air hammer.

Fig. 6e shows the effect of input air pressure on the impact frequency and impact energy per blow. Both the impact frequency and impact energy are improved when increasing the input air pressure. The increased input air pressure causes the augment in thrust on the piston, which can improve the acceleration of the piston, thereby increasing the impacting performance. The result data of the impact frequency obtained from CFD simulations are slightly different with that of the experimental results, demonstrating considerable agreement between them. Therefore, the accuracy and feasibility of this specific CFD approach is validated. The experimental data of the impact frequency are obtained by the analyses of the acoustic signal recorded using a microphone placed in the vicinity of the impacting system [24]. It can be found that improving the input air pressure can improve the penetration rate of the RC-DTH air hammer drilling; however, the diesel consumption will also increase simultaneously. Furthermore, for controlling the cost of RC-DTH air hammer drilling, the energy efficiency is an important indicator and can be calculated by the following equations:

$$\eta = \frac{P_{im}}{P_{in}} \tag{14}$$

where P_{in} is the input power of the air compressor that can be calculated as follows:

$$P_{in} = \dot{m} \int_{P_0}^{P_e} \frac{1}{\rho_0} \left(\frac{P_0}{P}\right)^{\frac{1}{k}} dP = \left(\frac{K}{K-1}\right) \dot{m} \frac{1}{\rho_0} P_0 \left[\left(\frac{P_e}{P_0}\right)^{\frac{K-1}{K}} - 1\right] \tag{15}$$
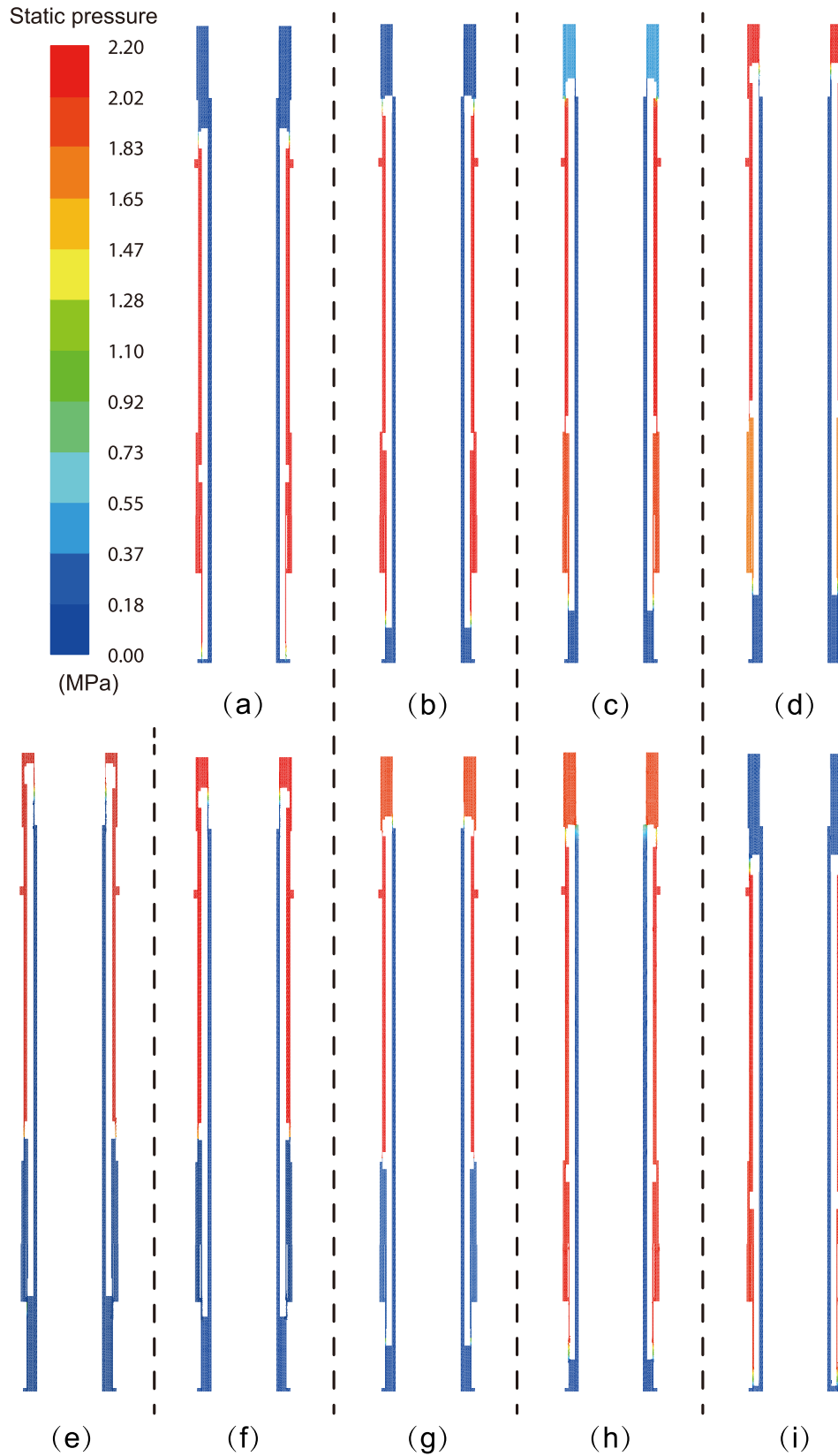
Fig. 5. Group of typical sectional pressure contours at nine instants. (a)–(i) correspond to the air stages in Fig. 3.

where $\dot{m}$ is the input air mass flow rate that can be obtained from the simulation results; P_e is the input air pressure; P_0 is the atmospheric pressure; ρ_0 is the air density at the standard condition that is 1.205 kg/m³; K is the adiabatic index that is 1.4 for air.

Fig. 6f shows the effects of input air pressure on the power output of the piston and the energy efficiency of the RC-DTH air hammer. As shown in Fig. 6e, both the impact frequency and impact energy per blow pose an increasing trend with increasing input
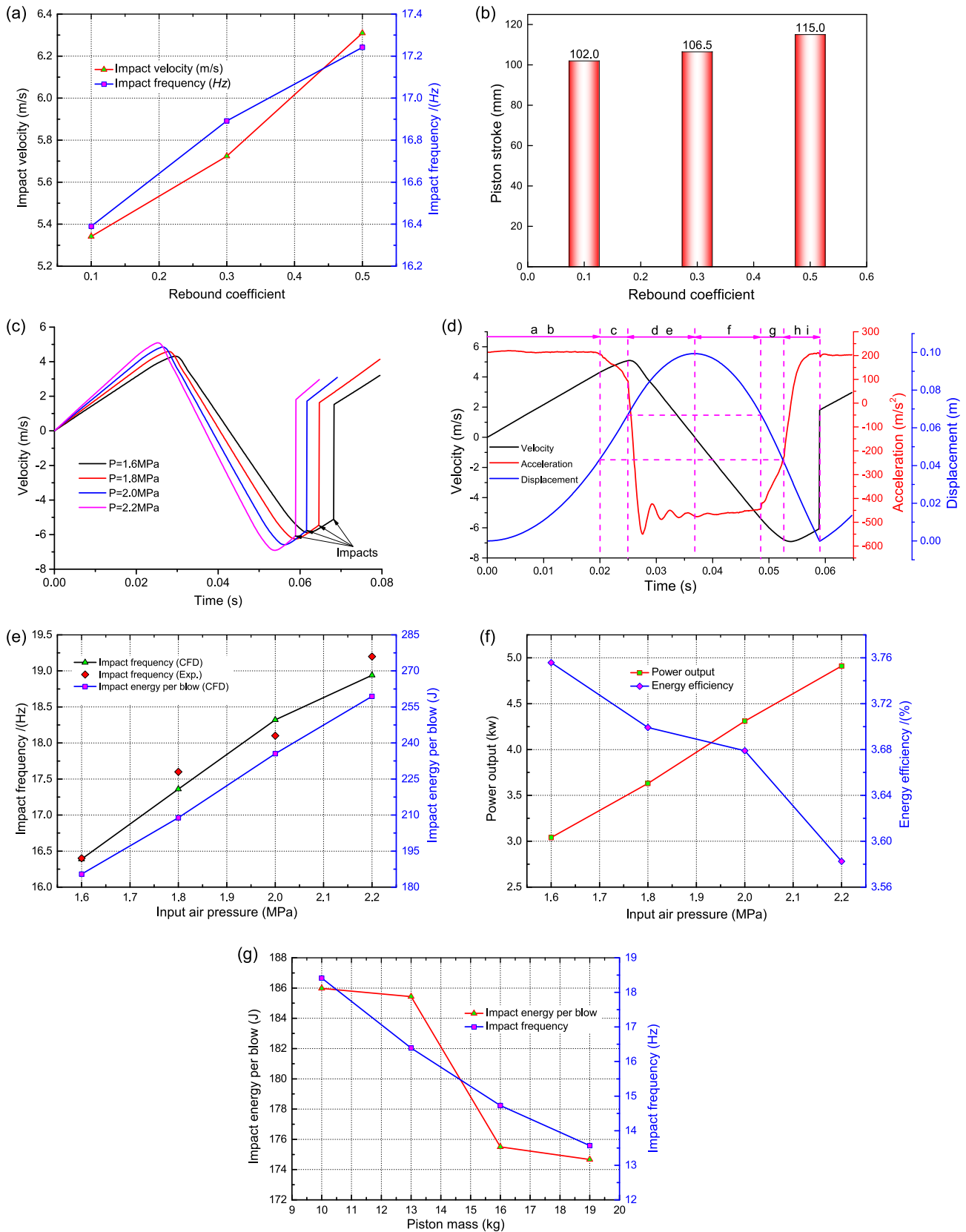
Fig. 6. Profiles obtained by CFD simulations. (a) effect of rebound coefficient on impact velocity and impact frequency; input air pressure is 1.6 MPa and piston mass is 13 kg; (b) effect of rebound coefficient on piston stroke; (c) piston velocity history obtained by CFD simulations; rebound coefficient is 0.3 and piston mass is 13 kg; (d) velocity, acceleration, and displacement histories of the piston obtained by CFD simulations; input air pressure is 2.2 MPa, rebound coefficient is 0.3, and piston mass is 13 kg; (e) effect of input air pressure on impact frequency and impact energy per blow; (f) effect of input air pressure on power output of piston and energy efficiency; and (g) effect of piston mass on impact frequency and impact energy per blow; input air pressure is 1.6 MPa and rebound coefficient is 0.3.

air pressure; hence, the power output increases accordingly. As expected, the energy efficiency decreases with increasing input air pressure. This phenomenon may be because the increased input air pressure requires more input volume flow rate of air to be compressed, which results in more conversion of heat energy. Additionally, a higher input air pressure causes more air leakage from the annular gaps between the cylindrical mating surfaces of the components, which will also reduce the energy efficiency.

Effects of piston mass on the performance of RC-DTH air hammer

When the input air pressure and rebound coefficient are given, the performance of the RC-DTH air hammer can also be influenced by changing the piston mass. Fig. 6g shows the effects of piston mass on the impact frequency and impact energy per blow. With the increase in the piston mass, both the impact frequency and impact energy per blow pose a decrease trend. When maintaining the input air pressure constant, increasing the piston mass would decrease the acceleration of the piston, thereby decreasing the piston velocity and impact frequency. In addition, as the piston mass increases, the increased motion period will cause more air leakage from the annular gaps between the cylindrical mating surfaces of components, which will decrease the impact energy per blow. As observed, a significant decrease in impact energy per blow occurs when the piston mass increases from 13 to 16 kg. This is because as the piston mass increases, the actual stroke decreases to less than L_{fie}, resulting in stage e being skipped, implying that the high-pressure air in the front chamber is not discharged in the entire stroke phase. This high-pressure-induced force in the front chamber decelerates the piston to some extent. Therefore, the selection of piston mass should be optimal to match with the designed geometric parameters.

Conclusions

A study on the performance of RC-DTH air hammers based on a CFD approach with the dynamic mesh method was proposed. The influence of rebound coefficient, input air pressure, and piston mass on the performance of the RC-DTH air hammer were studied numerically. The study results indicated that the increases in the rebound coefficient and input air pressure affected the impact performance of RC-DTH air hammers positively. With an input air pressure, increasing the piston mass would deteriorate the performance of the RC-DTH air hammers. The CFD approach with the dynamic mesh method was found to be effective and time saving with considerable accuracy and reliability. The design cycle of RC-DTH air hammers may be shortened significantly using this approach. However, the effects of geometric parameters in terms of L_{ro}, L_{fi}, L_{roc}, and L_{fie}, and the action areas of the piston are still unrevealed. Thus, further relevant studies are desired.

Conflict of interest

The authors have declared no conflict of interest

Compliance with Ethics Requirements

This article does not contain any studies with human or animal subjects.

Acknowledgements

References

[1] Kahraman S, Bilgin N, Feridunoglu C. Dominant rock properties affecting the penetration rate of percussive drills. Int J Rock mech Min 2003;40(5):711–23.
[2] Tuomas G. Effective use of water in a system for water driven hammer drilling. Tunn Undergr Sp Tech 2004;19(1):69–78.
[3] Han G, Bruno M, Dusseault MB. Dynamically modelling rock failure in percussion drilling. In: Presented at Alaska rocks 2005, the 40th US symposium on rock mechanics (USRMS): rock mechanics for energy, mineral and infrastructure development in the northern regions, Anchorage, Alaska; 2005 Jun 25–29.
[4] Santos H, Placido JCR, Oliveira JE, Gamboa L. Overcoming hard rock drilling challenges.
[5] Staysko R, Francis B, Cote B. Fluid hammer drives down well costs.
[6] Melamed Y, Kiselev A, Gelfgat M, Dreesen D, Blacic J. Hydraulic hammer drilling technology: developments and capabilities. J Energ Resour ASME 2000;122(1):1–7.
[7] Franca LFP. A bit-rock interaction model for rotary-percussive drilling. Int J Rock mech Min 2011;48(5):827–35.
[8] Ma Y, Guo X, Guo T, Huang R, Cai X, Li G. The puguang gas field: new giant discovery in the mature Sichuan basin, southwest china. AAPG Bull 2007;91(5):627–43.
[9] Yin K, Wang M, Peng J, Wang R. Percussion and rotary drilling. Beijing: Geological Publishing House; 2010.
[10] Strauss MF, Story SL, Mehlhorn NE. Applications of dual-wall reverse-circulation drilling in ground water exploration and monitoring. Ground Water Monit R 1989;9(2):63–71.
[11] Yin Q, Peng J, Bo K, He J, Kui Y, Gan X. Study on dust control performance of a hammer bit. Int Min Reclam Env 2013;27(6):393–406.
[12] Luo Y, Peng J, Li L, He J, Gan X, Yin K, et al. Development of a specially designed drill bit for down-the-hole air hammer to reduce dust production in the drilling process. J Clean Prod 2015;112:1040–8.
[13] Cao P, Chen Y, Liu M, Chen B. Optimal design of novel drill bit to control dust in down-the-hole hammer reverse circulation drilling. Arab J Sci Eng 2017;43(2):1–12.
[14] Wu D, Yin K, Yin Q, Zhang X, Cheng J, Ge D, et al. Reverse circulation drilling method based on a supersonic nozzle for dust Control. Appl Sci- Basel 2017;7(1):5.
[15] Wang M, Bai L, Wang L, Qiu S, Tian W, Su GH. Thermal hydraulic and stress coupling analysis for ap1000 Pressurized Thermal Shock (PTS) study under SBLOCA scenario. Appl Therm Eng 2017;122:158–70.
[16] Marschall KJ, Mleczko L. CFD Modeling of an internally circulating fluidized-bed reactor. Chem Eng Sci 1999;54(13):2085–93.
[17] Rahimi M, Parvareh A. CFD study on mixing by coupled jet-impeller mixers in a large crude oil storage tank. Comput Chem Eng 2007;31(7):737–44.
[18] Zhang X, Zhang S, Luo Y, Wu D. Experimental study and analysis on a fluidic hammer—an innovative rotary-percussion drilling tool. J Petrol Sci Eng 2019;173:362–70.
[19] Salehi S, Madani SA, Kiran R. Characterization of drilling fluids filtration through integrated laboratory experiments and CFD modeling. J Nat Gas Sci Eng 2016;29:462–8. 8.
[20] Wu D, Zhang S, He Y. A dynamic mesh-based approach to analyse hydrodynamic interactions between a fluidic hammer and drill bit. J Petrol Sci Eng 2019;175:536–46.
[21] Chen J, Yin K, Peng JM, Gu LY, Zhou B. Numerical simulation of the performance of the SC-89 jet impact system.
[22] Peng JM, Yin QL, Li GL, Liu H, Wang W. The effect of actuator parameters on the critical flow velocity of a fluidic amplifier. Appl Math Model 2013;37(14–15):7741–51.
[23] Zhang X, Peng J, Ge D, Bo K, Yin K, Wu D. Performance study of a fluidic hammer controlled by an output-fed bistable fluidic oscillator. Appl Sci – Basel 2016;6(10):305.
[24] Zhang X, Zhang S, Peng J, Wu D. A fluidic oscillator with concave attachment walls and shorter splitter distance for fluidic DTH hammers. Sens Actuators A – Phys 2018;270:127–35.
[25] Bao Y, Zhou D, Huang C, Wu Q, Chen XQ. Numerical prediction of aerodynamic characteristics of prismatic cylinder by finite element method with Spalart-Allmaras turbulence model. Comput Struct 2011;89(3):325–38.
[26] Celik IB, Ghia U, Roache PJ. Procedure for estimation and reporting of uncertainty due to discretization in CFD applications. J Fluid ENG-T ASME 2008;130(7):078001-1–4.
[27] Li X, Rupert G, Summers DA, Santi P, Liu D. Analysis of impact hammer rebound to estimate rock drillability. Rock Mech Rock Eng 2000;33(1):1–13.
[28] Simon R. Theory of rock drilling. Proc., sixth annual drilling symposium. University of Minnesota; 1956.